npj Climate and Atmospheric Science

Article in Press

An analytical framework reduces cloud feedback uncertainty by linking percentage cloud change to surface ocean warming patterns

Cite this article as: Ma, J., Feng, J., Su, H. *et al.* **An analytical framework reduces cloud feedback uncertainty by linking percentage cloud change to surface ocean warming patterns.** *npj Clim Atmos Sci* **(2026). https://doi.org/10.1038/s41612-026-01339-2**

Jian Ma, Jing Feng, Hui Su, Matthew Collins, Jing Su, In-Sik Kang, Masahiro Watanabe, Jianping Li & Yinding Zhang

We are providing an unedited version of this manuscript to give early access to its findings. Before final publication, the manuscript will undergo further editing. Please note there may be errors present which affect the content, and all legal disclaimers apply.

If this paper is publishing under a Transparent Peer Review model then Peer Review reports will publish with the final article.

An analytical framework reduces cloud feedback uncertainty by linking percentage cloud change to surface ocean warming patterns

Jian Ma[a,b], Jing Feng[c], Hui Su[d], Matthew Collins[e], Jing Su[a], In-Sik Kang[f], Masahiro Watanabe[g], Jianping Li[h,i], and Yinding Zhang[j]

[a]Yazhou Bay Innovation Research Institute, Hainan Tropical Ocean University; Sanya, Hainan, China

[b]College of Marine Science and Technology, Hainan Tropical Ocean University; Sanya, Hainan, China

[c]School of Oceanography, Shanghai Jiao Tong University; Shanghai, China.

[d]Department of Civil and Environmental Engineering, The Hong Kong University of Science and Technology; Hong Kong Special Administrative Region, China.

[e]Department of Mathematics and Statistics, University of Exeter; Exeter, UK.

[f]State Key Laboratory of Satellite Ocean Environment Dynamics, Second Institute of Oceanography, Ministry of Natural Resources; Hangzhou, Zhejiang, China.

[g]Atmosphere and Ocean Research Institute, University of Tokyo; Kashiwa, Chiba, Japan.

[h]Frontiers Science Center for Deep Ocean Multi-spheres and Earth System/Key Laboratory of Physical Oceanography/Academy of the Future Ocean, Ocean University of China; Qingdao, Shandong, China.

[i]Laboratory for Ocean Dynamics and Climate, Laoshan Laboratory; Qingdao, Shandong, China.

[j]School of Industrial Engineering, Purdue University; West Lafayette, IN, USA.

*Jian Ma and Hui Su

Email: majian@hntou.edu.cn; cehsu@ust.hk

Keywords: cloud feedback | warming patterns | emergent constraint | climate change

This PDF file includes:

Main Text
Methods
References
Figures 1 to 8

Abstract

Clouds significantly influence Earth's radiative balance with complex changes in response to surface warming. The key drivers of the changes are the sea surface temperature (SST) pattern effect that reshapes cloud distributions, and the beta feedback that scales low-level fraction change to climatological amounts. Cloud radiative feedback remains the largest source of uncertainty in future climate projections, but current constraints are insufficient. Here, we demonstrate that the percentage change in tropical cloud fraction, driven by spatial patterns SST increase, is linked to cloud height variations. We introduce a proportional warmer-get-higher paradigm and develop a pattern-based analytical framework, identifying three key factors governing cloud feedback: percentage cloud sensitivity to SST, climatological cloud cover, and SST warming patterns relative to the tropical mean. By leveraging recent observations to constrain these factors in two stages, we establish a process-oriented emergent constraint on projected cloud feedback in the 21st century. The first stage substitutes simulated cloud sensitivity and mean cloud cover to correct biases and reduce spread by half. Then, the second stage attempts to further constrain the SST pattern effect, which explains 79% of the remaining spread in an attribution procedure. This percentage framework yields total, low, middle, and high cloud feedback of 0.49±0.27, 0.33±0.21, 0.09±0.09, and 0.07±0.06 W m^{-2} K^{-1} (90% confidence), respectively. It reduces intermodel uncertainty by 59% for cloud feedback and 33% for surface warming, resulting in a climate sensitivity of 4.08±0.97 K.

Main Text

Introduction

As an important component of the global hydrological cycle, clouds exert a key influence over Earth's radiative energy budget (1). This process consists of the reflection of solar radiation by all clouds, and infrared absorption/emission mainly by clouds in the upper and mid-troposphere (2). Because cloud physics are complex in both convective and radiative contexts (3, 4), there is an enormous range of the cloud responses to the greenhouse effect in climate models (5). This leads to great uncertainty of the climate sensitivity, i.e., the projected future global warming after climate models have reached equilibrium with an imposed greenhouse gas increase (6). Decades of research have been devoted to constraining this cloud radiative feedback, including emergent constraints using observable statistics under the current climate to correct the model projections (7). However, recent studies have constrained low cloud feedback with different foci and results (8–10), such as 0.25±0.18 W m^{-2} K^{-1} over the tropical oceans, as well as 0.19±0.12 and 0.37±0.37 W m^{-2} K^{-1} in the near-global marine regions.

The diversity in both the methods and outcomes reflects the lack of a precise and clear understanding of cloud change processes. This study focuses on two distinct drivers among the many different mechanisms (6-10), some of which are widely accepted. On the one hand, the pattern effect of the sea surface temperature (SST) increase (11) describes the impact of temporally evolving spatial SST patterns on the radiative feedbacks and equilibrium climate sensitivity (12, 13) through reshaping the tropical hydrological cycle, with large uncertainty among climate models (14–17). In the Coupled Model Intercomparison Project (CMIP) phase 5, cloud feedback is most sensitive to the SST in the Indo-Pacific warm pool, while in CMIP6 it depends on all regions with robust SST pattern change (18). On the other

hand, the beta feedback of low-level cloud change (19) represents a local coupling between the boundary-layer cloud fraction, radiative cooling, and relative humidity based on spatially uniform SST warming (16). Hence, the strength of the low cloud radiative effects simulated in the current climate can largely determine the strength of the low cloud response to climate change. This results in a low cloud reduction proportional to climatology, with a strong negative correlation between them in regions where the mean-state cloud fraction is less than 40% (20). It is still unclear whether other types of clouds follow a similar scaling scheme.

Thus, achieving a consistent understanding across different model generations and cloud types remains a grand challenge. In this study, we introduce a new analytical framework to diagnose cloud feedback by examining the percentage change in cloud fraction relative to the climatological mean cloud cover. We find that this percentage change is approximately linearly related to the anomalous SST warming relative to the tropical mean, consistently between the observations and two generations of model projections. Notably, the correlations between anomalous SST and percentage cloud changes are opposite for high and low clouds, reflecting variations in cloud top height. Our percentage framework therefore proposes a proportional warmer-get-higher paradigm and identifies three key factors driving cloud radiative feedback.

Using Moderate Resolution Imaging Spectroradiometer (MODIS) cloud measurements (21, 22), converted radiative kernels (2), and a suite of SST observations (23), we constrain future projections from 7 CMIP5 and 14 CMIP6 models (24, 25). Employing an uncertainty attribution procedure, this stagewise emergent constraint efficiently reduces the intermodel spread of the 21 CMIP simulations. In the first stage, we indirectly link feedback uncertainty to historical cloud sensitivity to SST, substituting simulated sensitivity and present-day cloud cover to correct biases and reduce uncertainty by half. The second stage attempts to further constrain the SST pattern effect, explaining 79% of the remaining spread. Ultimately, our process-oriented constraint reduces uncertainty by 59% for cloud feedback and 33% for climate sensitivity. Validation during the historical period constrains tropical cloud feedback uncertainty to a quarter of the original range, aligning well with the observed feedback and demonstrating the robustness of our methodology.

Results

Systematic control of the SST patterns on percentage cloud change

We adopt abrupt CO_2 quadrupling (abrupt-4×CO2) runs by both the CMIP5 and CMIP6 models, and calculate the monthly changes as the differences in means between model years 1–10 and 131–140 (9). They are normalized by the global-mean increase in the surface (air) temperature, since climate feedback is defined as the net radiative response at the top of the atmosphere per unit of global warming. For

simplicity, we denote the normalized changes as δ and omit the common K^{-1} in the units. Cloud changes (26) involve the coverage (fraction, C), height (top pressure), and opacity (optical depth) of clouds. Summing through the optical depths, we categorize the cloud types according to top height into high (<440 hPa), middle (440–680 hPa), and low (>680 hPa) clouds. In passive satellite observations and simulators, apparent changes in low clouds can arise due to changes in higher-level clouds that reveal or obscure the underlying low clouds (9, 27), so we subsequently remove this obscuration effect (*Methods*).

In the tropical hydrological cycle, the SST warming patterns influence precipitation (14, 15) and circulation (16, 17) in a percentage manner, i.e., their changes are proportional to their climatological values. This convective effect on high clouds can be combined with the beta feedback of low clouds, to apply climatological modulation to the pattern effect for all cloud types. Thus, *Supplementary Materials* (Fig. S1) qualify that cloud fraction change is strongly influenced by SST patterns (T^*, relative SST increase deviating from the tropical mean warming) in terms of sign and by climatological amounts in terms of strength. Of course, cloud responses physically depend on where relative SST warming occurs (i.e., regions of climatological ascent or descent). Still, these regions are characterized by more high or low clouds in present climate, respectively. Therefore, δC exhibits various shifts from the SST patterns due to the $\overline{C}$-induced disparity in strength, which is even negligible for middle clouds (Fig. S1). Thus, our percentage framework implicitly considers the regional regimes using the climatological amount, as a local physical factor for cloud fraction change.

We therefore examine the percentage cloud change (Δ) in the tropics as the ratio of fraction change to climatological amount. The definition of the tropics extends to the subtropics, i.e., 40°S–40°N (28, 29), although spatial correlations increase for a narrower tropical band. Using overbars to indicate the annual and multi-model averages, Fig. 1 clearly reveals a pictorial spatial correlation (r_s) between the simulated $\overline{T^*}$ and $\overline{\Delta}$ patterns, in both sign and strength for high ($r_s = 0.56$) and low ($r_s = -0.58$) clouds. Similar to previous studies (15, 17), $\overline{T^*}$ features El Niño-like warming peaks in the eastern equatorial oceans and south-to-north gradients in the subtropical Pacific. Fewer low and more high clouds appear over the areas with relatively warmed SSTs, predicting a rise of cloud tops (15, 30) in proportion to the cloud climatology.

According to the definition of altitude change for total clouds (2, 26, 30), we refer to the above relationship as the proportional warmer-get-higher paradigm. However, different physical mechanisms may be at work for low clouds and high clouds separately. Cross-comparisons reveal that Δ has a reasonable advantage over δC. The tropical $\overline{\Delta}$ responds to $\overline{T^*}$ by the same order of magnitude for all cloud types (Fig. 1) and exhibits consistent vertical patterns in the troposphere (Fig. S2). Moreover, the oceanic zonal and equatorial meridional means of $\overline{\Delta}$ imply a potential competition between cloud regimes. That is, mid-level

clouds are associated with high clouds in the convective deep tropics, and with low clouds in the eastern equatorial and subtropical subsidence regions. Also shown in Fig. 1*B*, these changes represent their respective cloud regimes inside and outside ±15° latitudes, by similar scatters and strong r_s (0.62 and -0.4) with the SST patterns. The corresponding regression slopes are 22.2% K^{-1} and -10.2% K^{-1}, which is consistent with those of 16.9% K^{-1} and -8.5 % K^{-1} for high and low clouds, respectively. Such a distinction in regimes can result from the depth of convection (31) and have led to the negligible correlation for the entire tropics. This also indicates that the category of mid-level clouds is artificial and should be treated with caution. However, a region-specific cloud categorization is beyond the scope of this study, though it can be an interesting topic for future research. For now, we will continue to use the traditional definition of cloud types.

Pattern-based analytical framework using percentage cloud change

In order to attribute and constrain the uncertainty in cloud change and feedback, we develop a pattern-based percentage framework oriented by the above relationship (summarized as the first two steps in Fig. 2). The analytical definition for the patterns of percentage change in cloud fraction is

$$\Delta = \frac{\delta c}{\gamma}, \gamma = \begin{cases} C, & 40°\text{S} - 40°\text{N} \\ 1, & \text{Extratropics}' \end{cases} \tag{1}$$

where γ (unitless fraction) is a percentage parameter applied only to the tropical clouds, since Fig. S1 shows little influence of the large local C (%) on the generally weak δC (%) in the extratropics. Although this local denominator is small in some regions, it is still greater than zero. As shown in Fig. 1, land areas experience significant percentage cloud change for low and middle clouds due to minimal cloud coverage. However, these values are not extreme since cloud fraction change is weak where climatology is small.

The proportional warmer-get-higher paradigm suggests an empirical pointwise formulation between clouds and SST (15).

$$\Delta \approx \alpha \cdot T^* + \beta \langle \delta T_s \rangle, \tag{2}$$

where α (% K^{-1}) is defined as the percentage cloud sensitivity to the SST pattern change (8), and β (% K^{-1}) measures this to the global-mean surface warming ($\langle \delta T_s \rangle$ = 1 K after normalization). Separating the relative contributions of the pattern effect and overall warming, α and β are spatial constants only as a function of model and cloud type, ranging from positive for high clouds to negative for low clouds. Above the 99.99% confidence level, β has a strong mean rate of -2.3% K^{-1} (Fig. 1*C*) reflecting low cloud reduction due to overall warming (32). This is spatially proportional to the cloud climatology, manifested

by the beta feedback. This reduces global radiative cooling in favor of an overall positive feedback, driven by both radiative and latent heating via stability and entrainment (30, 33).

Furthermore, Fig. 3*A* exhibits wide ranges of α and β between models (8), which has also been found for regional precipitation changes (15). Our tests on stability indices (Fig. S4) indicates that these percentage sensitivities share similar relative strengths contributed by cloud-controlling factors (8, 9, 27, 28) within a given model. Therefore, α and β have a high intermodel correlation (r_m) of 0.71 for low clouds (0.62 and 0.83 for middle and high clouds, respectively), which allows us to predict $\beta \approx 0.29 \cdot \alpha$. This relationship can be inserted into Eq. **2** to obtain (see *Methods*)

$$\Delta \approx \alpha \cdot \left(T^* + \frac{\beta}{\alpha} \langle \delta T_s \rangle \right) \approx \alpha \cdot (T^* + T_0),$$ **[3]**

where $T_0 = \frac{\beta}{\alpha} \langle \delta T_s \rangle = 0.29 \langle \delta T_s \rangle = 0.29$ K for low clouds, which are 0.37 and 0.31 K for middle and high clouds, respectively. Regardless of the model, T_0 scales down the cloud response to the overall warming using pattern effect, replacing the model-dependent β and leaving only one sensitivity α to constrain. Combining Eqs. **1** and **3** quantifies that the cloud fraction change depends on both the SST patterns T^* (local and relative SST change) and the climatological amount γ (local physical factor), which is an insightful framework for integrating the pattern effect and beta feedback, respectively.

$$\delta C = \Delta \cdot \gamma \approx \alpha \cdot (T^* + T_0) \cdot \gamma.$$ **[4]**

Cloud feedback (λ) is typically calculated (2) from the product of fraction change and radiative kernels (K); however, the above percentage framework, inspired by our proportional warmer-get-higher, gives rise to an innovative redefinition of cloud feedback.

$$\lambda = \langle \delta C \cdot K \rangle = \langle \Delta \cdot \gamma K \rangle \approx \langle \alpha \cdot (T^* + T_0) \cdot \gamma K \rangle,$$ **[5]**

where $\langle \cdot \rangle$ denotes the feedback calculation, with a positive value of λ indicating positive cloud feedback. This explicitly discovers three key factors for the uncertainty in λ, namely cloud sensitivity (α), fractional kernels (γK), and T^*, which would be constrained in two stages. Since low clouds play a leading role in total cloud feedback (26), as shown in *Supplementary Materials* with Fig. S5, we take them as the main example for the following constraint.

Initial constraint with the observed cloud fraction and projected sensitivity

Adopting the MODIS clouds (22, 34) and averaged SST suite (23), the observed changes during 2003–2022 (Fig. 4) are calculated (*Methods*) using a Linear Inverse Model (LIM). The LIM is an empirical

dynamical model designed to minimize biases caused by interannual variability. The observations exhibit similar behaviors as the CMIP simulations in the tropical Pacific and Indian Ocean, but not in the Atlantic, which is likely due to internal decadal variability (35–37). Nevertheless, our warmer-get-higher paradigm remains robust, as indicated by the strong Δ-$\overline{T^*}$ relationship with opposite r_s values of 0.53 and -0.5 between high and non-obscured low clouds, respectively. Since the vertical patterns (Fig. S6) are similar but only noisier in the equatorial Pacific ($r_s = 0.75$) and northern tropics ($r_s = 0.51$), the observations agree with the simulations when comparing the consistency in the magnitude of Δ and the disparity in the strength of δC (modulated by C).

We then calculate the percentage cloud sensitivity from the above observations and use this α_o to construct an observational constraint on the rich diversity (-2 to –25%) of the percentage cloud sensitivity. As outlined by the last two steps in Fig. 2, Figs. 3 and 4 are utilized to generate Figs. 5 to 7. The CMIP historical simulations are more consistent with the observations over time than abrupt-4×CO2. Therefore, we switch to this scenario and calculate the low cloud sensitivity (α_h) for changes between 1986–1995 and 1996–2005, as shown in Fig. 3B. We then scatter α_h from the history with α into the future, which exhibits a close relationship ($r_m = 0.86$), to ensure the robustness in between. The observed sensitivity has a low cloud average ($\alpha_o = $ -6.7% K^{-1}) near the center of the historical range (-1 to -18% K^{-1}), which can be projected via linear regression of α against α_h. The resulting α_p (-7.39% K^{-1}) is slightly weaker than the ensemble-mean α (-8.5% K^{-1}) for abrupt-4×CO2 (Fig. 1C). Incidentally, the intercept in the short-term observations (Fig. 4C) drops to about half of that of the abrupt-4×CO2 simulations.

The projected sensitivity, α_p, can now be used to constrain the α-induced uncertainty. As shown in Fig. 3C, low cloud α contributes 48% ($r_m = $ -0.69) of the spread in global total cloud feedback, based on a strong intermodel correlation (0.92) between the tropical and global feedbacks (Fig. S7). Here, three outlier models weaken the contribution, but are shown in *Supplementary Materials* to hardly affect our constraint and included in the final results. We apply a scaling substitution that multiplies Eq. **5** by the ratio $\frac{\alpha_p}{\alpha}$ for all cloud types in each experiment (see *Methods* and Fig. S2). This is equivalent to substituting the projected observations α_p for simulated model α. According to our analytical framework, it should eliminate the uncertainty and bias associated with percentage cloud sensitivity in cloud feedback.

$$\lambda_s = \langle \Delta_s \cdot \gamma_o K \rangle = \langle \frac{\alpha_p}{\alpha} \Delta \cdot \gamma_o K \rangle \approx \langle \alpha_p \cdot (T^* + T_0) \cdot \gamma_o K \rangle, \qquad \textbf{[6]}$$

where the subscript *s* denotes substituted or scaled, *o* marks observed, and *p* means projected. It can be seen that Eq. **6** also constrains γK in Eq. **5** by replacing the simulated γ with the observed γ_o (pattern

comparisons are shown in Fig. S8). However, the SST patterns have not yet been constricted and remain as shown in Fig. S1D.

Our initial constraint reduces the uncertainty and biases in λ via α in sensitivity and γ in pattern, deriving a more reasonable λ_s (Fig. 5). This is as if λ_s were computed from the observed mean state with reliable projected sensitivity, but perturbed by the original uncertainty in modeled T^*. Such an observational substitution has the distinct advantage of intuitively correcting common model biases in the fractional kernels that induce large and noisy λ over the tropical oceans (Fig. 5A), e.g., due to the excessive equatorial cold tongue (16). This leads to more positive and the most uncertain patterns of λ_s preferentially in the eastern tropical basins (Fig. 5B), suggesting stronger non-obscured reductions in low clouds modulated by its observed climatology. Eq. **6** also greatly attenuates the original feedback and nearly removes its uncertainty elsewhere, including the negative and diverse signals in the convective regions and high latitudes of the North Atlantic. Especially, the zonal mean patterns show that feedback effects of middle and high clouds above 680 hPa are almost eliminated in terms of both the mean and spread.

These turn the original global cloud feedback of 0.49±0.65, 0.26±0.3, 0.12±0.37, and 0.11±0.13 W m^{-2} K^{-1} (Fig. S5) to the substituted feedback of 0.45±0.3, 0.3±0.24, 0.08±0.11, and 0.07±0.13 W m^{-2} K^{-1} (90% confidence) for total, low, middle, and high clouds, respectively. Fig. 7C compares λ_s with λ to show its uncertainty reductions of 69% and 19% for middle and low clouds, respectively. This halves the range of total cloud feedback and reduces its mean by 0.04 W m^{-2} K^{-1}, mainly due to higher-level clouds, but mitigated by an equal increase in low cloud feedback.

Attribution of cloud feedback uncertainty to the SST patterns

The observational constraint on the percentage cloud sensitivity to SST patterns and mean cloud cover are sufficient to reduce more than half of the uncertainty in total cloud feedback. We now further constrain the global cloud feedback by constricting the SST patterns themselves (T^*). Indeed, the spatial mean of SST patterns is defined to be zero, but fractional kernels can assign unequal weights in Eqs. **5** and **6**, creating a global radiative imbalance. Moreover, there is great uncertainty (Fig. 1D) in T^* (15), which can

thus be incorporated into cloud feedback, allowing the pattern effect to profoundly perturb the climate sensitivity (11, 12, 13, 35).

To quantify this, we decompose λ_s using our percentage analytical framework to design an attribution procedure (see *Methods*). This can demonstrate component reductions in feedback uncertainty by the initial constraint and further constrain the substituted feedback.

$$\lambda_s = \langle \overline{\Delta_s} \cdot \gamma_o \overline{K} \rangle + \langle \overline{\Delta_s} \cdot \gamma_o K' \rangle + \langle \Delta_s'^* \cdot \gamma_o \overline{K} \rangle + \langle \Delta_s'^* \cdot \gamma_o K' \rangle + \langle \Delta_s'_R \cdot \gamma_o K \rangle, \qquad [7]$$

where the overbars and primes denote ensemble means and intermodel anomalies, K' is interpolated for each model from the surface shortwave albedo along longitude, $\Delta_s'^*$ is the anomalous scaled percentage cloud change (Δ_s') driven by T^*, and $\Delta_s'_R$ is the residual factors, including the inversion strength (12, 28) and optical depth (9, 38). The last term introduces noise into Eqs. **2** to **6**, so we use the approximate equal sign ($\approx$).

Instead of evaluating Eqs. **6** and **7** for each model, we obtain $\Delta_s'^*$ via intermodel singular value decomposition (SVD) between T^* and Δ_s' across the globe. This quantifies the SST pattern effect on the percentage cloud change for individual models. To avoid overreliance on either variable, we provide covariant spatio-model modes between the two (15, 29, 39, 40). The SVDs are applied to both the scaled Δ_s and unscaled Δ, presenting similar modes in reasonably shifted orders (*Supplementary Materials*, Fig. S9 and *Methods*). We then adopt these results to perform two sets of attributions using Eqs. **7** and **12**, for λ_s with and λ without the initial constraint. In turn, the terms on the right-hand side represent the product of the ensemble averages including T_0, biases in the fractional kernels, uncertainty induced by the SST patterns, nonlinear interaction between the two, and the residual effect.

Since the cumulative variance of SVD reconstruction converges after the ~11 leading modes, we accumulate the first 12 modes to represent the T^* effects (17) in both λ_s (Fig. S10) and λ (see *Methods*). A comparison of these attributions between Fig. 6 and Fig. S11 clearly shows how the initial constraint halves the uncertainty in total cloud feedback. The 90% confidence intervals of T^* and the residual terms are reduced by 55% and 43%, respectively, and the kernel and interaction terms are largely eliminated, as is expected. The latter is similar for all of the cloud types, while the former varies, leading to different uncertainty reductions. As a result, the T^* contribution to the intermodel variance drops from 82% for λ to 79% for λ_s, and the residuals explain 21%. The kernel biases account for 18% of the uncertainty in λ. The decompositions for the cloud types largely agree with that of total cloud feedback (Fig. 6), recognizing the

residual factors as a secondary contributor and the SST patterns as the primary. The sum of all of the factors recovers 100% of the total uncertainty.

Eventual constraint attempted for the SST pattern effect

SVD mode 1 (Fig. S9 *A* to *C*) shows a prominent T^* feature in 30°S–30°N, correlated with the climatological fraction of low plus middle clouds (Fig. S1 *B* + *C*; r_s = 0.33), and the fractional net kernel (Fig. S8*C*; r_s = -0.34). This establishes a link between the SST patterns and climatological cloud radiative effects in space, implying air-sea feedback against the backdrop of a spatially uniform SST increase. The fraction of low clouds decreases in proportion to the present-day fraction (19, 20), indicating rapid dissipation in the subsidence rather than convective regions. Therefore, surface solar heating increases more in the equatorial cold tongue and northeastern subtropical Pacific, which drives the anomalous warming patterns. Such an initial SST anomaly scales with climatological cloud radiative effects and can lead to further evolution (e.g., meridional gradients in SVD mode 2) of the equilibrium (41) SST patterns (Fig. S1*D*). Reasonably, the magnitude of this local feedback is also adjusted by the percentage cloud sensitivity, as revealed by its strong intermodel correlation with the principal components (PCs) of mode 1: 0.51 and 0.57 (0.46 and 0.52 with the outlier models) for SST and clouds, respectively. Thus, our percentage analytical framework allows the sensitivity diversity to play a key role in tuning SST patterns, generating up to 32% of the large uncertainty among models.

The above implication inspires the eventual constraint (Fig. 2), based on recent observations of percentage cloud sensitivity. We regress the LIM-perturbed low cloud Δ in the non-obscured MODIS dataset, against T^* from each member of the SST suite. The 90% confidence interval of these sensitivity estimates indicates the uncertainty range of α_o (see Fig. 3*B*). The range is then projected onto α_p through the previously established regression of α against α_h. This leads to an uncertainty range that is slightly narrower than that of α_o. It constricts the nine runs (filled symbols in Fig. 3*C*), which were performed using three CMIP5 and six CMIP6 models. We postulate that these models have more reliable α values to project some reasonable magnitudes of the local cloud feedback and determine the most likely T^*. We finally complete the emergent constraint with the attribution procedure according to Eq. **7**. In particular, the three terms related to the SST pattern effect are extracted from these models; however, the residual factors should remain unchanged (see *Methods*). Therefore, the dominant T^* term is constrained to the values of the nine models in Fig. 6. Compared to Fig. S11, its uncertainty is reduced by 35%, 6%, 40%, and 43% for total, low, middle, and high clouds, respectively.

In total, the constrained cloud feedback in Fig. 7*A* is more positive than that in Fig. 5*B*, and the maxima still remain in the low cloud regions, where the intermodel uncertainty is further reduced and is mainly

confined to the eastern tropical ocean basins. Compared to the original T^* (Fig. S1D), the constricted one (Fig. 7B) exhibits generally weakened patterns, except for the Southern Ocean warming. Nevertheless, these SSTs look close in the ensemble mean because they share the same SVD modes; whereas, the tropical spread is much reduced by the constriction using the nine models that have similar amplitudes for the cloud-triggered mode. The global high, middle, low, and total cloud feedback (Fig. 7C) becomes 0.07±0.06, 0.09±0.09, 0.33±0.21, and 0.49±0.27 W m^{-2} K^{-1} (90% confidence), respectively. Examining the outlier models at the end of *Supplementary Materials* reveals a marginal effect on our constraint, so we keep them in the final results. This also reflects the great robustness of our method.

Aligned with the literature, our non-obscured low cloud feedback is similar to the multi-evidence work (9, 10) and median-tight effort (8) in the ensemble mean and uncertainty, respectively. However, our pattern-based percentage framework consistently constrains global radiative feedback across all of the cloud types, rather than just low clouds. In detail, it applies to the entire cloud fraction histogram with different scaling between pressure levels, explicitly addressing the amount and altitude feedbacks simultaneously. Furthermore, *Supplementary Materials* exhibit that our approach can implicitly adjust optical depth feedback (see Fig. S12). For instance, high cloud altitude feedback remains positive during our constraint because of rising cloud tops. However, this is mitigated by negative optical depth feedback, which results from increased solar reflection due to thickening high clouds (26). Such a decrease in feedback of -0.04 by high clouds reinforces the -0.03 by middle clouds, to offset the increase of 0.07 W m^{-2} K^{-1} by low clouds. Thus, our constraint keeps the mean unchanged for total cloud λ while significantly reducing its uncertainty by 59%, as significant improvements from 0.27±0.41 and 0.45±0.54 W m^{-2} K^{-1} (9, 10).

Validating our methodology and constraining climate sensitivity

Given the increasing complexity of the statistical analysis for observational constraints on cloud feedback, a validation is necessary to make a convincing case (9, 37). Therefore, we follow the precedent of recent studies to validate our two-stage emergent constraint by applying it to the historical simulations in the tropics, where T^* differs from the future. These results are compared with cloud feedback based on the observations (Fig. 8), where the aerosol-cloud interaction is important. However, it cannot be removed for either observations or simulations, so we do not distinguish this aerosol effect from cloud feedback. The historical shortwave kernel is calculated with the corresponding albedo, and the observational kernels are taken from an interannual reanalysis (42). The MODIS cloud change in Fig. S6 A and B is used to

compute the radiative effect, normalized by the tropical-mean warming from the SST suite, which provides the uncertainty.

In Fig. 8, the observed tropical feedback (90% confidence) of total clouds is 0.55±0.11 W m^{-2} K^{-1}, which is consistent with the global feedback of 0.57±0.71 W m^{-2} K^{-1} when the effects of changing water vapor, surface and atmospheric temperature, surface albedo, and radiative forcing are subtracted from the top-of-atmosphere flux (43). This is dominated by low clouds (0.49±0.1), with insignificant contributions from middle (-0.05±0.01) and high (0.11±0.02 W m^{-2} K^{-1}) clouds. In contrast, the original historical cloud feedback has a very small ensemble mean but extremely large intermodel variability (90% confidence), i.e., 0.07±2.98, -0.18±1.75, 0.13±0.89, and 0.12±0.67 W m^{-2} K^{-1}. This bias from the observations is rapidly reduced by the substituted feedback of 0.87±0.88, 0.8±0.83, 0.14±0.17, and -0.07±0.36 W m^{-2} K^{-1}. Finally, the constrained feedback can well cover the observed range for the strong total (0.69±0.53) and low (0.56±0.47) cloud feedback, and closely overlaps with that for the weak middle (0.23±0.17) and high (-0.1±0.24 W m^{-2} K^{-1}) cloud feedback. This not only dramatically reduces total cloud feedback uncertainty by 82%, but also fully validates our percentage framework and stagewise constraint.

Our pattern-based percentage framework effectively constrains total cloud feedback — consisting of those due to amount, altitude, and optical depth — across the globe via strong relationship between the tropical and global feedbacks. Therefore, we can confidently constrain the effective equilibrium climate sensitivity using constrained cloud feedback (9, 13). This is estimated as the x intercept divided by two (as if under 2×CO2) after regressing the global-mean and annual-mean anomalies of the net downwelling radiative flux at the top of the atmosphere on those of the surface temperature, where both anomalies are calculated between the abrupt-4×CO2 scenario and the averaged piControl over years 91–140. It is highly correlated ($r_m = 0.8$) with the global total cloud λ, so its uncertainty can be reduced with our constrained net feedback. The hierarchical emergent constraint method is applied under the assumption of Gaussian distributions of the intermodel spreads (44). This leads to an unaffected mean of 4.08 K, and a 35% reduction in the spread from ±1.29 K to ±0.84 K (66% confidence), which is more effective than the 25% reduction from the latest study (9). At the 90% confidence level, the reduction is 33% from 4.08±1.44 K to 4.08±0.97 K, consistent with, but tighter than, a combined estimate of 4.0±1.07 K with a large overconfidence based on several emergent constraints (45).

Discussion

By integrating the pattern effect and beta feedback, which have previously been considered in isolation, this study reveals the systematic control of the percentage change in cloud fraction due to effect of the tropical SST patterns. A proportional warmer-get-higher paradigm is then proposed to tightly constrain the global radiative feedback for all cloud types. The main sources of intermodel variability are identified as

the percentage cloud sensitivity, present-day simulation biases, and regional SST change. We first address the former two by substituting the historical-projected observed sensitivity and MODIS cloud fraction and then try an observational constraint on the latter factor based on an uncertainty attribution procedure. The constrained uncertainty in total cloud feedback reaches about two-fifths of the original, but the mean value remains unchanged, suggesting that the feedback extremes are less likely to be valid. For the equilibrium climate sensitivity, this constraint translates into about two-thirds of the original uncertainty, again leaving the mean unchanged.

Our validation results based on the historical simulations cover the observed range of the significant cloud feedback well, with an extreme uncertainty reduction of about three quarters, indicating a successful emergent constraint. Nevertheless, future changes in the SST patterns are highly uncertain (10, 46–52), which cannot be fully constrained by α alone, as is evident in Fig. 7*B* with a peak in the North Atlantic. This reflects that the nine constricted models may have deficiencies in other areas, such as ocean dynamics, mean state SST biases, additional atmospheric processes, and atmosphere-ocean interactions (53). To further resolve such spread and improve the reliability of climate projections, SST pattern formation under global warming needs to be re-examined. For this, our pattern-based analytical framework for percentage cloud change may provide an insightful perspective as a unique trigger of air-sea interactions.

Methods

SST and cloud observations. The SST observations (23) are adopted from the MODIS, Hadley Centre Sea Ice and SST (HadISST), Extended Reconstructed (ERSST) v5, Optimum Interpolation (OISST) v2, and Centennial Observation-Based Estimates (COBESST) v1. Among these, MODIS provides retrievals from two polar-orbiting satellites, Terra and Aqua, that sample at different times of day (morning and afternoon) and night (before and after midnight) at a given location. We create a data suite of all of the SST products to analyze their mean and uncertainty. Combining the Aqua and Terra cloud observations, MODIS releases a Level-3 CFMIP Observation Simulator Package (MCD06COSP). It facilitates comparison between climate models and satellite observations by producing synthetic MODIS data from the model integrations, e.g., the cloud property histogram (22). Cloud fraction is given separately for partly cloudy scenes and for overcast scenes, which we add together to obtain cloud fraction for all cloud scenes, based on the recently corrected v6.2 dataset.

We use the monthly products covering 2003–2022 and process them into a spatial resolution of 1° latitude by 2° longitude. The SST and cloud changes are computed using an LIM to minimize the biases caused by interannual variability (23). The LIM is an empirical dynamical model that treats spatially varying climate anomalies as a combination of the predictable dynamics plus an unpredictable nonlinear

white noise. Approximated using a stochastically forced linear dynamical system, the time evolution of a climate variable is determined from the observed state vector, expressed in a reduced space of empirical orthogonal function (EOF). These EOFs have been obtained separately for each field, and the 20 leading PCs are input to the LIM. The lag-covariance for the linear dynamical operator is then computed using a training lag of 11 months, to which the results are generally insensitive. The least damped eigenmode of the LIM operator varies the slowest, so it is ultimately captured as the externally forced trend. The LIM provides detrended PC simulations to generate noise-induced perturbations for the trend. Thus, we generate 500 realizations to estimate the uncertainty in the MODIS cloud observations regressed against the SST suite.

Admittedly, the observations do not use exactly the same criteria for interpreting cloud top pressure as clisccp in the models (21), e.g., many mid-level clouds retrieved by the satellite simulator are assigned lower heights by MODIS. This upward shift in simulated cloud tops can cause potential problems in the development of emergent constraints (9); however, the actual satellites retrieve cloud height about correctly, so our methodology can indeed resolve the error. In addition to replacing the mean-state cloud fraction in the models with the observations, we also scale the magnitude of the simulated cloud response with the observed percentage cloud sensitivity, both of which correct for the level shifts of the cloud observations. The only variable that we have not replaced with the observations is the SST patterns, which is not height dependent. All these distinctive features of our stagewise constraint would lead to reasonable cloud changes and result in an effective constraint. The only possible bias could be in the sign of middle cloud change, which might be influenced more by low clouds and less by high clouds.

Multi-scenario CMIP output. Given the limited availability of the cloud property histogram (clisccp) variable (2), we analyze the SST and cloud changes in 21 runs using 7 CMIP5 and 14 CMIP6 models (24, 25) under the preindustrial control (piControl) and abrupt CO_2 quadrupling (abrupt-4×CO2) scenarios, as well as 20 historical simulations without the unavailable CCSM4. The models (Fig. S3) provide clisccp and other changes for robust quantitative assessments of cloud feedback and climate sensitivity.

CMIP6: CanESM5, CESM2-FV2*, CNRM-CM6-1, CNRM-ESM2-1, E3SM-1.0, E3SM-2.0, E3SM-2.0-NARRM, GFDL/CM4, HadGEM3-GC3.1-LL, MIROC6, MIROC-ES2L, MRI-ESM2.0, UKESM1.0-LL, and UKESM1.1-LL;

CMIP5: CanESM2, CCSM4*, HadGEM2-ES, MIROC5, MIROC-ESM, MPI-ESM-LR, and MRI-CGCM3.

*Historical simulations: CESM2 is found instead of CESM2-FV2; and CCSM4 is not available.

We adopt the monthly output of one realization from each simulation and interpolate all of the fields to a 2° latitude by 2.5° longitude grid prior to analysis. Averaged over years 91–140, the piControl runs are used to calculate the abrupt-4×CO2 anomalies for estimating the climate sensitivity. The abrupt-4×CO2

experiments are at least 140 years long (except for 104 years of CCSM4), and the changes are defined as the differences between the last and first 10-year long means. The historical simulations cover the periods 1850–2014 in CMIP6 and 1850–2005 in CMIP5. We select a mutual 20-year period of 1986–2005 for comparison with the observations during 2003–2022. It is assumed that such a year shift would not affect the results, which is supported by the high r_m value (0.83) for low cloud α_h from the CMIP6 runs between 1995–2014 and 1986–2005. For a consistent relationship with α under abrupt-4×CO2, the changes are defined in the same way.

Cloud feedback is expressed as the response of the top-of-atmosphere net radiative flux to the changes per unit of global-mean surface air warming; therefore, the cloud changes are normalized accordingly before computing the ensemble means, uncertainties, spreads, correlations, regressions, and SVDs. In addition, the SST patterns are normalized by the global-mean increase in the surface temperature ($\langle \delta T_s \rangle$), which differs from the air warming by only -0.02±0.07 K. For simplicity, the normalized changes are marked by δ, and the common K^{-1} in their units is omitted. The 90% (66%) confidence interval (e.g., of cloud feedback) is calculated as ±half of the 5–95 (17–83) percentile range of the values across the simulations (9).

Cloud feedback computed using radiative kernels. The clisccp variable, endorsed by the Cloud Feedback Model Intercomparison Project (CFMIP), represents a 7 by 7 histogram of cloud properties along the top pressure (p) and optical depth (τ). Summations in its matrix or submatrices can classify total or each type of clouds to calculate the corresponding fraction (C) in the climatology or change (δC), as well as cloud feedback (λ). By summing throughout τ, we categorize the cloud types according to p.

(a) High clouds: 0–440 hPa (pressure levels 5–7), all optical depths;
(b) Middle clouds: 440–680 hPa (pressure levels 3–4), all optical depths;
(c) Low clouds: 680–1000 hPa (pressure levels 1–2), all optical depths;
(d) Total clouds: 0–1000 hPa (all pressure levels), all optical depths.

The passive satellite sensors and simulators report the top pressure of the highest clouds in the column, allowing an amount increase of higher-level clouds to obscure more of low-level clouds. This reduces low cloud amount retrieved by the satellite, even if it does not actually change (27). Here we remove this obscuration effect (9) by separating the real low cloud changes from the artificial changes in the satellite data.

$$\begin{cases} l_n = \frac{l}{1-U} \\ U = \sum_{p=3}^{p=7} \sum_{\tau=1}^{\tau=7} c \end{cases} \implies \begin{cases} \delta c_n = (1 - \bar{U}) \, \delta l_n \\ c_n = (1 - \bar{U}) \, \bar{l}_n \end{cases}, \qquad \text{[8]}$$

where $c = c_{p\tau}$ denotes clisccp, $l = l_{p\tau}$ is the retrieved low-level cloud fraction, U is the higher-level cloud amount (cloud fraction summed over all τ bins and the non-low-level p bins), l_n is the non-obscured low-level cloud fraction, $\overline{U}$ and $\overline{l_n}$ are the climatological monthly means of U and l_n, and δl_n is the normalized monthly change in l_n. This yields non-obscured histograms of cloud fraction actually used for low clouds, i.e., c_n and δc_n in climatology and change, respectively.

The cloud radiative kernels (2) convert the clisccp change per unit of global-mean surface air warming into its corresponding radiative effect, quantifying cloud feedback across the various models as a reliable and consistent methodology. They use the incremental monthly cloud change to describe the differential response of the top-of-atmosphere shortwave and longwave fluxes. Such conversions act as spatial weights for the changes in the cloud properties to calculate the global feedback as follows:

(a) Normalize the changes in cloud histogram using the global-mean surface air warming;
(b) Interpolate the shortwave kernel with the surface albedo (upward/downward clear-sky shortwave flux) in each model along longitude;
(c) Multiply the histogram changes by the longwave and interpolated shortwave kernels;
(d) Perform summation along pressure and/or optical depth for total and each cloud type;
(e) Average annually over 12 months and horizontally over the globe.

The entire procedure is denoted by $\langle \cdot \rangle$, such as $\lambda = \langle \delta C \cdot K \rangle$ in Eq. **5**, where λ is defined as positive for positive feedback from clouds.

Intermodel statistical analysis. This statistical analysis explores the dynamical interpretations for tracing the valuable sources of uncertainty, e.g., the contribution of the percentage cloud sensitivity to cloud feedback. Regular statistics use spatiotemporal fields as inputs, but here we replace the time axis with the model series to perform intermodel analysis. In particular, the intermodel correlations and regressions are performed for cloud feedback, and the variances explained by different factors are estimated as the exclusive R^2 (to be introduced) for the total effect. In addition, Student's t-tests are used to assess the confidence of the correlations using the following formula:

$$t_r = \frac{\sqrt{n-3}}{2} \ln\left(\frac{1+r}{1-r}\right),$$ **[9]**

where t_r is the test statistic derived from the correlation r (r_s or r_m) and the sample size n. All of r_m across the 21 models are above the 90% confidence level. Except for the (percentage) fraction change in total and middle clouds, all of r_s pass the 99.99% confidence tests because the tropical sample size is at least 4430 for the SST patterns or 270 for the zonal-mean cloud fraction.

As an extension of the EOF, the SVD analysis (21, 22) is a popular multivariate statistical method, which uses two variables as inputs to identify their patterns with the maximum covariance. Here we perform

intermodel SVD (23, 24) to extract the effect of the SST patterns on the regional cloud changes with their covariant modes. Two sets of SVDs are applied to the monthly intermodel anomalies of Δ and Δ_s in Eqs. **5** and **6**, respectively. They are both between the global T^* (4-D: *x*, *y*, month, model) and cloud changes (6-D: *x*, *y*, *p*, τ, month, model) in terms of the percentage for the extended tropics (40°S–40°N) and the fraction for the outside extratropics. All of the variables have been concatenated into 2-D matrices with dimensions only along the model and the combinations of others, and the ensemble mean is removed for each grid box. A covariance matrix $Co = \Delta^t T^* / N$ is then constructed by eliminating the common model dimension, where *t* denotes the transpose operator and *N* represents the number of models.

The SVD function converts Co into a tuple of three arrays *E*, Σ, and *F*. Each column in *E* contains a singular vector for Δ, as does *F* for T^*, while Σ contains the singular values not used here. These orthonormal singular vectors are identified as the spatial modes and are projected onto each of the variables to define the corresponding PCs, which are also model-dependent. We then use the fractional kernels to compute the partial feedback due to the cloud patterns in each of the SVD modes, and we multiply it by the corresponding PC. This reconstructs the T^*-related intermodel variability in cloud feedbacks associated with these modes, which are ranked according to the individual variances (direct R^2) they explain for the intermodel uncertainty in the total cloud feedback. Finally, the multi-model partial feedbacks reconstructed by the leading SVD modes are linearly combined to quantify their cumulative variance (25) using the exclusive R^2 method below.

Uncertainty attribution procedure for cloud feedback. Based on our analytical framework inspired by the warmer-get-higher paradigm, we redefine cloud feedback in terms of percentage fraction change in the tropics. Here, the definition of the tropics includes the subtropics, with a latitudinal range of about 35°S–35°N. According to the American Meteorological Society, this can extend further poleward on west coasts of continents, e.g., prominent δC patterns shown in Fig. S1 reach 40° over the eastern ocean basins. Thus, we define the extended tropics as 40°S–40°N to better represent thermally driven dynamics (28, 29).

Eq. **5** identifies key drivers of the uncertainty in cloud feedback by distinctly integrating the physical processes of the pattern effect and beta feedback in the extended tropics. The percentage change in cloud fraction is mainly controlled by the SST patterns, and its sensitivity varies between the models. This is independent of the cloud climatology, which introduces the biases of the mean-state simulation into the cloud fraction change. To obtain this in detail, Eq. **3** is derived from Eq. **2** and Fig. 3*A*:

$$\left.\begin{array}{l} \Delta \approx \alpha \cdot T^* + \beta \left\langle \delta T_s \right\rangle \\ \beta \approx 0.29 \cdot \alpha - 1.91 \approx 0.29 \cdot \alpha \end{array}\right\} \Rightarrow \begin{array}{l} \Delta \approx \alpha \cdot T^* + 0.29\,\alpha \cdot 1\,\mathrm{K} \\ = \alpha \cdot T^* + \alpha \cdot 0.29\,\mathrm{K} \\ = \alpha \cdot (T^* + T_0) \end{array} . \qquad \textbf{[10]}$$

We believe that the intercept of -1.91% K^{-1} is negligible (54, 55). It is less than the standard deviation (2.26 % K^{-1}) of β and only about 22% (Fig. 3A) of its wide range (-0.7 to -8% K^{-1}).

Eq. **5** transforms the product of cloud fraction change (δC) and radiative kernels (K) into that of the percentage change (Δ) and fractional kernels (γK), which can be further decomposed.

$$\begin{cases} \Delta = \overline{\Delta} + \Delta' = \overline{\Delta} + \Delta'^* + \Delta'_R, \\ \gamma K = \overline{\gamma K} + (\gamma K)' \end{cases},$$

[11]

where the overbars and primes denote the ensemble means and intermodel anomalies, and Δ'^* and Δ'_R are the components of Δ' induced by T^* and the residual factors, respectively. It should be noted that we use the approximate equal sign ($\approx$) in the above equations about Δ to imply the noise introduced by Δ'_R. In order to quantify the contributions of factors such as the T^* spread and the γK biases, an uncertainty attribution procedure can be derived for the redefined global cloud feedback as follows:

$$\lambda = \langle (\overline{\Delta} + \Delta'^* + \Delta'_R) \cdot [\overline{\gamma K} + (\gamma K)'] \rangle,$$

$$\Rightarrow \lambda = \langle \overline{\Delta} \cdot \overline{\gamma K} \rangle + \langle \overline{\Delta} \cdot (\gamma K)' \rangle + \langle \Delta'^* \cdot \overline{\gamma K} \rangle + \langle \Delta'^* \cdot (\gamma K)' \rangle + \langle \Delta'_R \cdot \gamma K \rangle.$$

[12]

Similarly, the substituted feedback λ_s in Eq. **6** can be decomposed as in Eq. **7**, where Δ_s and γ_o replace Δ and γ, and the treatment of $\gamma_o K$ is slightly adjusted from Eq. **11**: $\gamma_o K = \gamma_o \overline{K} + \gamma_o K'$.

The SST pattern effect is obtained using the intermodel SVDs mentioned above (Fig. S9). In Figs. S10 and S11 and Fig. 6, the factor contributions are quantified slightly differently. The former only examines the cloud feedback anomalies associated with the ensemble-mean factional kernels ($\langle \Delta_s' \cdot \gamma_o \overline{K} \rangle$). The dominant influences of the T^* term ($\langle \Delta_s'^* \cdot \gamma_o \overline{K} \rangle$) converge to 77% for λ_s and 86% for λ, both after the ~11 leading SVD modes. In contrast, the latter two quantitatively attribute the feedback to all of the intermodel terms, e.g., $\langle \overline{\Delta_s} \cdot \gamma_o K' \rangle$, $\langle \Delta_s'^* \cdot \gamma_o \overline{K} \rangle$, $\langle \Delta_s'^* \cdot \gamma_o K' \rangle$, and $\langle \Delta_s'_R \cdot \gamma_o K \rangle$. This in turn leads to 18%, 82%, 0%, and 0% for Eq. **12**, as well as 0%, 79%, 0%, and 21% for Eq. **7**. In both cases, the sum of all of the factors fully recovers the total uncertainty. The attributions elaborate how the spread in cloud feedback is reduced by the initial constraint: substituted to 45% and 57% for total clouds, the ranges of the T^* and residual terms experience different reductions among the cloud types; the kernel and interaction terms are almost eliminated in all cases as is expected.

Process-oriented emergent constraint in two stages. Applied to cloud sensitivity, present-day simulation biases, and regional SST change, our stagewise emergent constraint on the global cloud feedback employs an uncertainty attribution procedure, based on the analytical framework for percentage cloud change. Fig. 2 illustrates how to substitute the projected observations α_p for the simulated

sensitivity α of Δ regressed on T^* at each cloud height, as well as γ_o for γ, and how to constrict the SST patterns using the observational range.

After summing the annual-mean clisccp and its changes over all optical depths, we carry out a percentage calculation, spatial correlation, and linear regression of Δ against T^* in the tropics. Hence, the percentage cloud sensitivity is obtained at seven pressure levels for the abrupt-4×CO2 experiments (α), historical simulations (α_h), and averaged observations (α_o). We then perform linear regression of α against α_h, based on their high r_m value of 0.86, and use this to project α_o onto α_p. A 7-level ratio of $\left|\frac{\alpha_p}{\alpha}\right|$ is calculated for each of the 21 models and is multiplied by the global Δ from the 7-by-7 clisccp according to Eq. **6**, except for those that are weakly correlated with T^* ($|r_s| < 0.15$, mostly middle clouds). Based on the linear relationship with α, the cloud sensitivity to the spatial-mean surface warming (β in Fig. 3A) is implicitly scaled by the same factor. Additionally, cloud fraction γ_o observed by MODIS is used to replace the climatology γ in the tropical fractional kernels (γK in Eq. **5**) simulated by each model. These form the initial stage of our emergent constraint, represented by Eq. **6**. This reduces the uncertainty and biases in λ via α in sensitivity and γ in pattern to derive a more reasonable λ_s, as if computed from the observed mean state using a reliable projected sensitivity (Figs. 5 and 7C).

The uncertainty in the observed percentage cloud sensitivity α_o is also estimated for non-obscured low clouds and projected onto the future. We perform 500 LIM simulations to perturb the regression slope of the MODIS Δ against the T^* from the eight members of the SST suite, and then, we obtain the 90% confidence interval over the 4000 sensitivities. The projection of this range via the above regression of α against α_h leads to a smaller uncertainty in α_p, which contains nine values of the simulated sensitivity α. They result from the models that can project some most likely T^*, namely, CanESM2, HadGEM2-ES, and MPI-ESM-LR (CMIP5), as well as CNRM-CM6-1, CNRM-ESM2-1, GFDL/CM4, HadGEM3-GC3.1-LL, UKESM1.0-LL, and UKESM1.1-LL (CMIP6). On the right-hand side of Eq. **7**, we use these models for the three terms related to the SST patterns: $\langle \overline{\Delta_s} \cdot \gamma_o K' \rangle$, $\langle \Delta_s'^* \cdot \gamma_o \overline{K} \rangle$, and $\langle \Delta_s'^* \cdot \gamma_o K' \rangle$. However, the first ($\langle \overline{\Delta_s} \cdot \gamma_o \overline{K} \rangle$) and last ($\langle \Delta_s'_R \cdot \gamma_o K \rangle$) terms are unrelated to the uncertainty in T^* and hence unchanged. In this way, the eventual stage of our emergent constraint utilizes the attribution procedure expressed by Eq. **7** to constrict the uncertainty of T^* and fully retain the residual perturbations (Fig. 6).

In particular, the first term represents the product of the two ensemble means, which is free of intermodel variability. Therefore, it is added to the summed means of the rest of the terms for the ensemble-mean feedback (Fig. 6), but is excluded from the intermodel uncertainty (U), which is evaluated as follows:

$$U = \sqrt{U^2_{\langle \overline{\Delta_s} \cdot \gamma_o K' \rangle_9 + \langle \Delta_s'^* \cdot \gamma_o \overline{K} \rangle_9 + \langle \Delta_s'^* \cdot \gamma_o K' \rangle_9} + U^2_{\langle \Delta_s'_R \cdot \gamma_o K \rangle_{21}}}. \qquad \textbf{[13]}$$

We first sum the three SST-related terms from the 9 (subscripted) constricted models and obtain their uncertainty at the 90% (66%) confidence level, calculated as ±half of the 5–95 (17–83) percentile range (9). Since the simulation choice appears abrupt, this is bootstrapped 1,000 times to increase the sample size. The substitution reserves 65%, 94%, 60%, and 57% of the uncertainty in the dominant T^* term among these models, giving values of ±0.2, 0.16, 0.08, and 0.04 W m^{-2} K^{-1} (90% confidence; gray error bars in Fig. 6) for total, low, middle, and high cloud feedback, respectively. The uncertainty in the last term is then derived similarly from all 21 (subscripted) models without bootstrapping, yielding values of ±0.18, 0.14, 0.05, and 0.04 W m^{-2} K^{-1} (90% confidence; blue in Fig. 6). Finally, Eq. **13** results in the constrained uncertainty of ±0.27, 0.21, 0.09, and 0.06 W m^{-2} K^{-1} (90% confidence; black in Fig. 6). Overall, our stagewise emergent constraint reduces the intermodel range of the global total cloud feedback by 59% (Fig. 7).

Variances explained by linearly interdependent factors. Here we develop an exclusive R^2 method to solve the overfitting problem in the variance explanations of the linearly interdependent factors for the cloud type decompositions and uncertainty attributions. For example, the sum of the variances (direct R^2) explained by the cloud types exceeds 1 for the global shortwave feedback (Fig. S5*A*). To correct this, we need to remove the part that is repeatedly counted in the different factors due to their linear dependence. This study involves the situations with 2–4 factors.

$Z = A + B$ is the simplest case, with two factors. The results of the exclusive R^2 method are denoted as R_A^2 and R_B^2 for A and B, respectively, and the direct R^2 values (squared correlations) are denoted as $R^2(Z, A)$ and $R^2(Z, B)$. The repetitive part between A and B is double counted (2×1) in $R^2(Z, A) + R^2(Z, B)$, so it is expressed as $R_{AB}^2 = \frac{R^2(Z,A)+R^2(Z,B)-1}{2}$. With the sum guaranteed to be 1, the exclusive R^2 can be obtained as follows:

$$\begin{cases} R_A^2 = R^2(Z,A) - R_{AB}^2 = \frac{1+R^2(Z,A)-R^2(Z,B)}{2} \\ R_B^2 = R^2(Z,B) - R_{AB}^2 = \frac{1-R^2(Z,A)+R^2(Z,B)}{2} \end{cases}$$

[14]

In the three-factor case, the common part between A, B, and C is overcounted by 6 (3×2) times in $R^2(Z, A) + R^2(Z, B) + R^2(Z, C)$, and that between any two factors is counted twice. For four factors, the overcounting of the part common to all of them increases to 12 (4×3), and those for fewer factors remain the same as in the simpler cases. Consequently, the maximum overcounting of the common part would reach $i \times (i - 1)$ in the case with i factors. All of the situations can be treated in a similar way to the two-factor case, although the mathematical procedures should become increasingly complicated.

Data Availability: The CMIP output at phases 5 and 6 is archived at https://aims2.llnl.gov/search/ and https://data.ceda.ac.uk/badc. The cloud radiative kernels can be accessed at

Code Availability: The MATLAB, NCO, Ferret, and Python codes used to process and analyze these data can be obtained by contacting the corresponding author.

Author Contributions: J.M. and J.F. are the co-first authors: J.M. designed research and wrote the paper; J.F. performed analyses. H.S. arranged methodology. M.C., I.S.K., M.W., and J.L. revised the paper. J.S. performed the SVD and Y.Z. assisted.

Competing Interests: I.S.K. and M.W. are affiliated with this journal as Editors or Editorial Board Members. The other authors do not have a competing interest.

References

1. D. L. Hartmann, M. E. Ockert-Bell, M. L. Michelsen, The effect of cloud type on earth's energy balance: global analysis. *J. Clim.* 5, 1281–1304 (1992).

2. M. D. Zelinka, S. A. Klein, D. L. Hartmann, Computing and partitioning cloud feedbacks using cloud property histograms. Part I: Cloud radiative kernels. *J. Clim.* 25, 3715–3735 (2012).

3. S. C. Sherwood, S. Bony, J.-L. Dufresne, Spread in model climate sensitivity traced to atmospheric convective mixing. *Nature* 505, 37–42 (2014).

4. C. Zhou, M. D. Zelinka, S. A. Klein, Impact of decadal cloud variations on the Earth's energy budget. *Nat. Geosci.* 9, 871–874 (2016).

5. I. Tan, T. Storelvmo, M. D. Zelinka, Observational constraints on mixed-phase clouds imply higher climate sensitivity. *Science* 352, 224–227 (2016).

6. B. Stevens, S. C. Sherwood, S. Bony, M. J. Webb, Prospects for narrowing bounds on Earth's equilibrium climate sensitivity. *Earth's Future* 4, 512–522 (2016).

7. S. A. Klein, A. Hall, Emergent constraints for cloud feedbacks. *Curr. Clim. Change Rep.* 1, 276–287 (2015).

8. S. A. Klein, A. Hall, J. R. Norris, R. Pincus, Low-cloud feedbacks from cloud-controlling factors: A review. *Surv. Geophys.* 38, 1307–1329 (2017).

9. T. A. Myers *et al.*, Observational constraints on low cloud feedback reduce uncertainty of climate sensitivity. *Nat. Clim. Change* 11, 501–507 (2021).

10. S. C. Sherwood *et al.*, An assessment of Earth's climate sensitivity using multiple lines of evidence. *Rev. Geophys.* 58, e2019RG000678 (2020).

11. C. Zhou, M. D. Zelinka, S. A. Klein, Analyzing the dependence of global cloud feedback on the spatial pattern of sea surface temperature change with a Green's function approach. *J. Adv. Model. Earth Syst.* 9, 2174–2189 (2017).

12. P. Ceppi, P. Nowack, Observational evidence that cloud feedback amplifies global warming. *Proc. Natl. Acad. Sci. USA* 118, e2026290118 (2021).

13. G. V. Cesana, A. D. del Genio, Observational constraint on cloud feedbacks suggests moderate climate sensitivity. *Nat. Clim. Change* 11, 213–218 (2021).

14. S.-P. Xie *et al.*, Global warming pattern formation: Sea surface temperature and rainfall. *J. Clim.* 23, 966–986 (2010).

15. J. Ma, S.-P. Xie, Regional patterns of sea surface temperature change: A source of uncertainty in future projections of precipitation and atmospheric circulation. *J. Clim.* 26, 2482–2501 (2013).

16. J. Ma *et al.*, Responses of the tropical atmospheric circulation to climate change and connection to the hydrological cycle. *Annu. Rev. Earth Planet. Sci.* 46, 549–580 (2018).

17. J. Zhang, J. Ma, J. Che, Z.-Q. Zhou, G. Gao, Surface warming patterns dominate the uncertainty in global water vapor plus lapse rate feedback. *Acta Oceanol. Sin.* 39, 1–9 (2020).

18. Y. Dong *et al.*, Intermodel spread in the pattern effect and its contribution to climate sensitivity in CMIP5 and CMIP6 models. *J. Clim.* 33, 7755–7775 (2020).

19. F. Brient, S. Bony, How may low-cloud radiative properties simulated in the current climate influence low-cloud feedbacks under global warming? *Geophys. Res. Lett.* 39, L20807 (2012).

20. H. Zhang *et al.*, Low-cloud feedback in CAM5-CLUBB: Physical mechanisms and parameter sensitivity analysis. *J. Adv. Model. Earth Syst.* 10, 2844–2864 (2018).

21. R. Pincus, S. Platnick, S. A. Ackerman, R. S. Hemler, R. J. P. Hofmann, Reconciling simulated and observed views of clouds: MODIS, ISCCP, and the limits of instrument simulators. *J. Clim.* 25, 4699–4720 (2012).

22. R. Pincus *et al.*, Updated observations of clouds by MODIS for global model assessment. *Earth Syst. Sci. Data* 15, 2483–2497 (2023).

23. T. Xu *et al.*, An increase in marine heatwaves without significant changes in surface ocean temperature variability. *Nat. Commun.* 13, 7396 (2022).

24. K. E. Taylor, R. J. Stouffer, G. A. Meehl, An overview of CMIP5 and the experiment design. *Bull. Am. Meteorol. Soc.* 93, 485–498 (2012).

25. V. Eyring *et al.*, Overview of the Coupled Model Intercomparison Project Phase 6 (CMIP6) experimental design and organization. *Geosci. Model Dev.* 9, 1937–1958 (2016).

26. J. Feng, J. Ma, Improved decomposition of cloud feedback and corresponding pattern change under uniform surface ocean warming: I. Anomalous mean method. *Geosci. Lett.* 12, 35, doi:10.1186/s40562-025-00407-4 (2025).

27. R. Scott *et al.*, Observed sensitivity of low-cloud radiative effects to meteorological perturbations over the global oceans. *J. Clim.* 33, 7717–7734 (2020).

28. T. Koshiro, H. Kawai, A. T. Noda, Estimated cloud-top entrainment index explains positive low-cloud-cover feedback. *Proc. Nat. Acad. Sci.* 119, e2200635119 (2022).

29. J. Ma, S.-P. Xie, Y. Kosaka, Mechanisms for tropical tropospheric circulation change in response to global warming. *J. Clim.* 25, 2979–2994 (2012).

30. I. N. Williams, R. T. Pierrehumbert, Observational evidence against strongly stabilizing tropical cloud feedbacks. *Geophys. Res. Lett.* 44, 1503–1510 (2017).

31. P. Good *et al.*, High sensitivity of tropical precipitation to local sea surface temperature. *Nature* 589, 408–414 (2021).

32. I. N. Williams, R. T. Pierrehumbert, M. Huber, Global warming, convective threshold and false thermostats. *Geophys. Res. Lett.* 36, L21805 (2009).

33. T. Schneider, C. M. Kaul, K. G. Pressel, Possible climate transitions from breakup of stratocumulus decks under greenhouse warming. *Nat. Geosci.* 12, 163–167 (2019).

34. C. Zhou, M. D. Zelinka, A. E. Dessler, P. Yang, An analysis of the short-term cloud feedback using MODIS data. *J. Clim.* 26, 4803–4815 (2013).

35. K. D. Williams, W. J. Ingram, J. M. Gregory, Time variation of effective climate sensitivity in GCMs. *J. Clim.* 21, 5076–5090 (2008).

36. M. Watanabe *et al.*, Contribution of natural decadal variability to global-warming acceleration and hiatus. *Nat. Clim. Change* 4, 893–897 (2014).

37. C. J. Wall *et al.*, Assessing effective radiative forcing from aerosol-cloud interactions over the global ocean. *Proc. Natl. Acad. Sci. USA* 119, e2210481119 (2022).

38. M. D. Zelinka *et al.*, Causes of higher climate sensitivity in CMIP6 models. *Geophys. Res. Lett.* 47, e2019GL085782 (2020).

39. Q. Hu, On the uniqueness of the singular value decomposition in meteorological applications. *J. Clim.* 10, 1762–1766 (1997).

40. H. Murakami *et al.*, Detected climatic change in global distribution of tropical cyclones. *Proc. Natl. Acad. Sci. USA* 117, 10706–10714 (2020).

41. U. K. Heede, A. V. Fedorov, N. Burls, A stronger versus weaker Walker: understanding model differences in fast and slow tropical Pacific responses to global warming. *Clim. Dyn.* 57, 2505–2522 (2021).

42. C. Zhou, Y. C. Liu, Q. Wang, Calculating the climatology and anomalies of surface cloud radiative effect using cloud property histograms and cloud radiative kernels. *Adv. Atmos. Sci.*, 39, 2124–2136 (2022).

43. A. E. Dessler, N. G. Loeb, Impact of dataset choice on calculations of the short-term cloud feedback. *J. Geophys. Res.*, 118, 2821–2826 (2013).

44. H. Shiogama, M. Watanabe, H. Kim, N. Hirota, Emergent constraints on future precipitation changes. *Nature*, 602, 612–616 (2022).

45. C. S. Bretherton, P. M. Caldwell, Combining emergent constraints for climate sensitivity. *J. Clim.* 33, 7413–7430 (2020).

46. D. L. Hartmann, The Antarctic ozone hole and the pattern effect on climate sensitivity. *Proc. Natl. Acad. Sci. USA* 119, e2207889119 (2022).

47. U. K. Heede, A. V. Fedorov, Eastern equatorial Pacific warming delayed by aerosols and thermostat response to CO_2 increase. *Nat. Clim. Change* 11, 696–703 (2021).

48. Y. Kostov, D. Ferreira, K. C. Armour, J. Marshall, Contributions of greenhouse gas forcing and the Southern Annular Mode to historical Southern Ocean surface temperature trends. *Geophys. Res. Lett.* 45, 1086–1097 (2018).

49. C. D. Rye *et al.*, Antarctic glacial melt as a driver of recent Southern Ocean climate trends. *Geophys. Res. Lett.* 47, e2019GL086892 (2020).

50. R. Seager *et al.*, Strengthening tropical Pacific zonal sea surface temperature gradient consistent with rising greenhouse gases. *Nat. Clim. Change* 9, 517–522 (2019).

51. M. Watanabe, J.-L. Dufresne, Y. Kosaka, T. Mauritsen, H. Tatebe, Enhanced warming constrained by past trends in equatorial Pacific sea surface temperature gradient. *Nat. Clim. Change* 11, 33–37 (2021).

52. R. C. J. Wills, Y. Dong, C. Proistosecu, K. C. Armour, D. S. Bars, Systematic climate model biases in the large-scale patterns of recent sea-surface temperature and sea-level pressure change. *Geophys. Res. Lett.* 49, e2022GL100011 (2022).

53. S.-P. Xie *et al.*, Towards predictive understanding of regional climate change. *Nat. Clim. Change* 5, 921–930 (2015).

54. A. Hall *et al.*, Progressing emergent constraints on future climate change. *Nat. Clim. Change* 9, 269–278 (2019).

55. P. M. Caldwell *et al.*, Statistical significance of climate sensitivity predictors obtained by data mining. *Geophys. Res. Lett.* 41, 1803–1808 (2014).

Figures
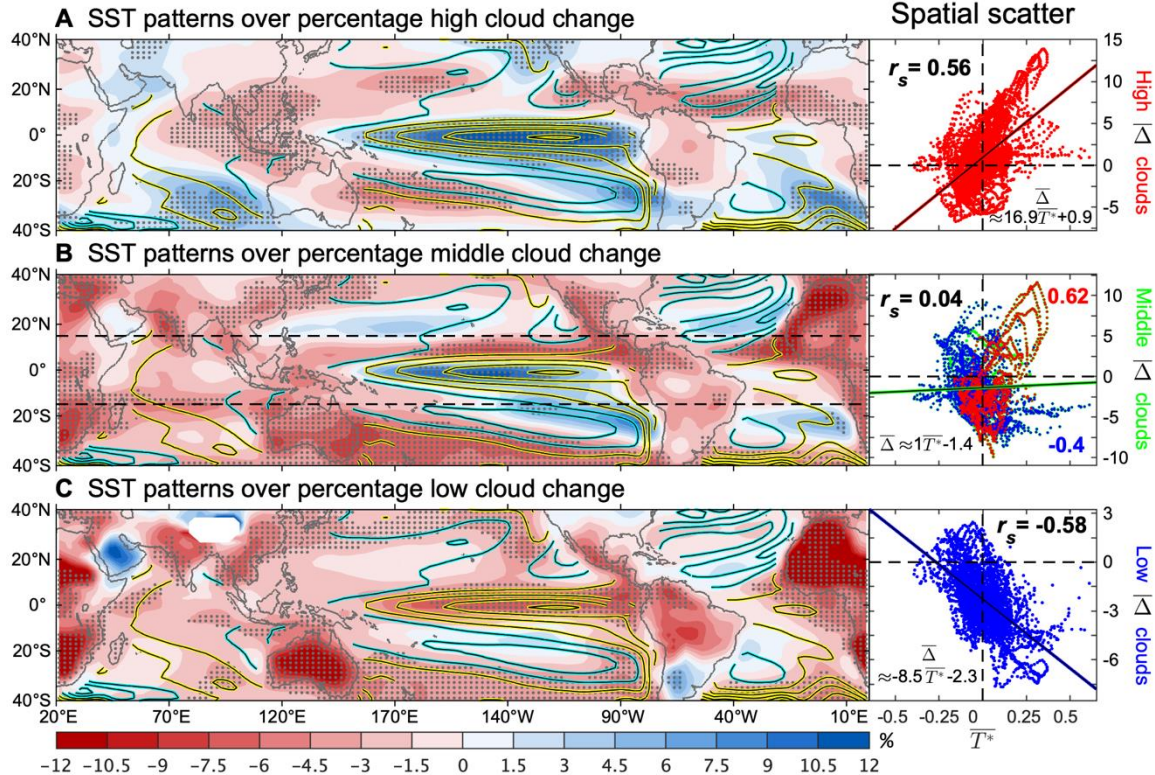
Figure 1. Comparisons of the horizontal distributions between the model ensemble-mean tropical SST change patterns $\overline{T^*}$ [contours, contour interval (CI): 0.1 K; yellow positive, cyan negative; 0 omitted] and the mean percentage change in cloud fraction $\overline{\Delta}$ (shading, %).

They are accompanied by spatial scatterplots (right) for (*A*) high (red), (*B*) middle (green), and (*C*) low (blue) clouds. In the left panel, $\overline{\Delta}$ is beyond the intermodel spread of Δ in the stippled areas, while the right panel also lists the spatial correlations and regression coefficients (% K^{-1}) of $\overline{\Delta}$ vs. $\overline{T^*}$. In (*B*), mid-level cloud changes in the deep tropics and subtropics (inside and outside ±15° latitudes, separated by dashed lines) are highlighted and individually correlated with $\overline{T^*}$, to represent the high (red) and low (blue) cloud regimes, respectively. Here we use the 21 CMIP simulations normalized by the global-mean surface (air) warming. Implying the changes in the top heights, high and low clouds are positively and negatively correlated with the SST patterns, respectively, and the spatial scatters and correlations exhibit their competitive control over mid-level clouds.
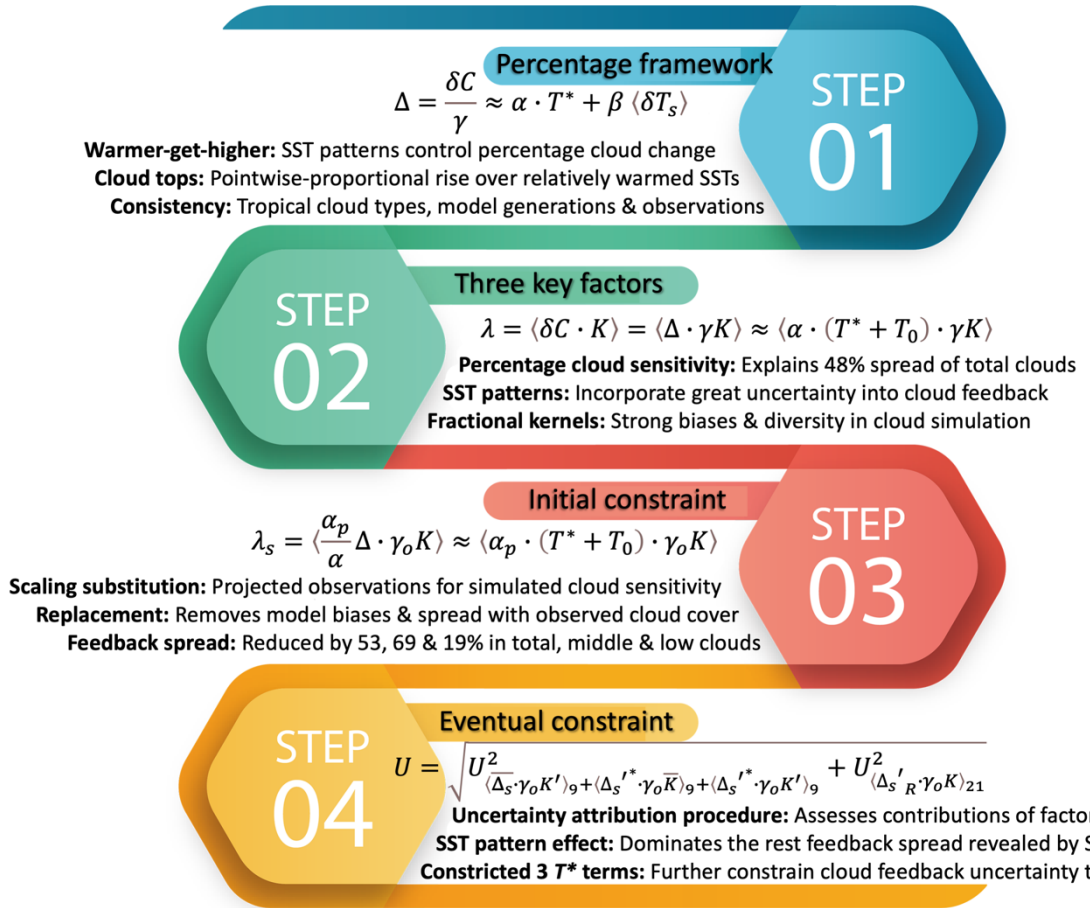
Figure 2. A flowchart outlining our pattern-based analytical framework for percentage cloud change and a two-stage, process-oriented emergent constraint.

The first two steps summarize our warmer-get-higher paradigm and the three main drivers of cloud feedback uncertainty. The last two steps first constrain the uncertainty in cloud feedback by scaling the percentage cloud sensitivity and substituting the observed cloud fraction. Finally, the SST pattern effect is constricted with the uncertainty in the projected observational sensitivity.
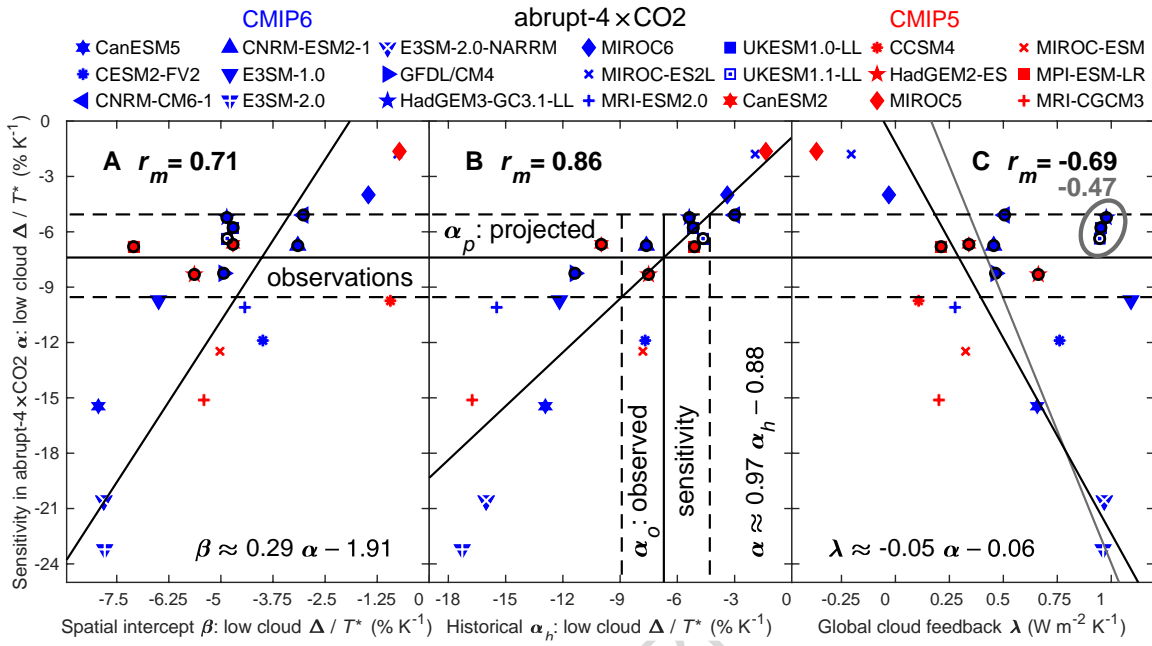
Figure 3. Intermodel scatterplots of the percentage cloud sensitivity α, i.e., the slope (% K^{-1}) in the tropical regression of low cloud Δ against T^*, and other important parameters.

They include (*A*) the spatial intercept β (% K^{-1}), (*B*) the historical sensitivity α_h (% K^{-1}), and (*C*) the global radiative feedback λ (W m^{-2} K^{-1}) for total clouds. The average (vertical solid bar) and uncertainty (90% confidence; dashed lines) of the observed sensitivity α_o are computed from the LIM and its noise perturbations, respectively, for the MODIS clouds regressed against the SST suite. The intermodel *y-x* (*x-y* in *B*) correlations and regressions are marked, which project the observed sensitivity α_o onto a projected sensitivity α_p in (*B*), including both the mean (horizontal solid bar) and spread (dashed lines). In (*C*), the gray r_m represents the correlation across all 21 models, but the black one and regression coefficients are calculated without three outlier models encircled in gray. Here we use the monthly-mean radiative kernels, SST and cloud observations, and 21 CMIP simulations normalized by the global-mean surface (air) warming. The percentage cloud sensitivity to the SST patterns is highly correlated with that to the global-mean surface warming, as a major contributor to the uncertainty in cloud feedback for most models, and all models can be constrained by the projected observational sensitivity that constricts nine simulations (circled in black) using its projected range.
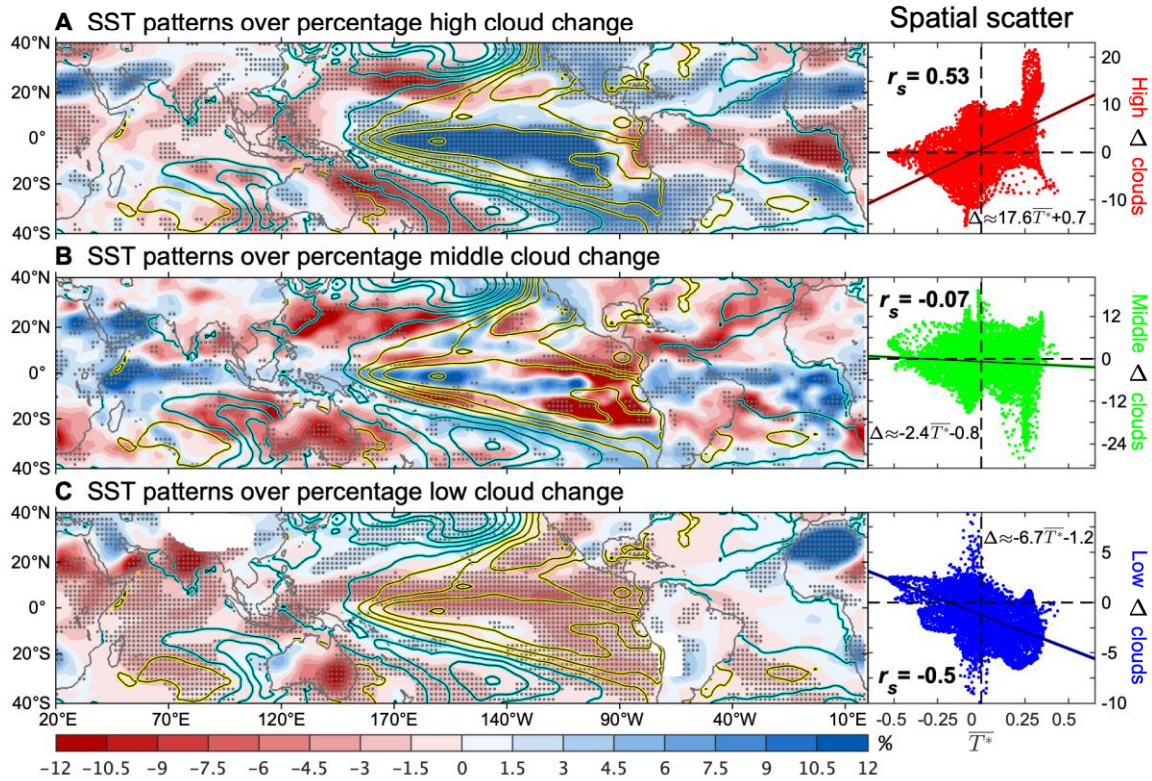
Figure 4. Same as in Fig. 1 but computed with the MODIS clouds and the averaged SST observations for 2003–2022 using the LIM.

The stippling indicates that the trend mode is beyond the spread in the LIM noise perturbations. Similar to the model projections in the tropical Pacific and Indian Oceans, the changes in spatial patterns from the observations exhibit a robust warmer-get-higher relationship between the $\overline{T^*}$ and Δ, with their correlations opposite in high and low clouds.
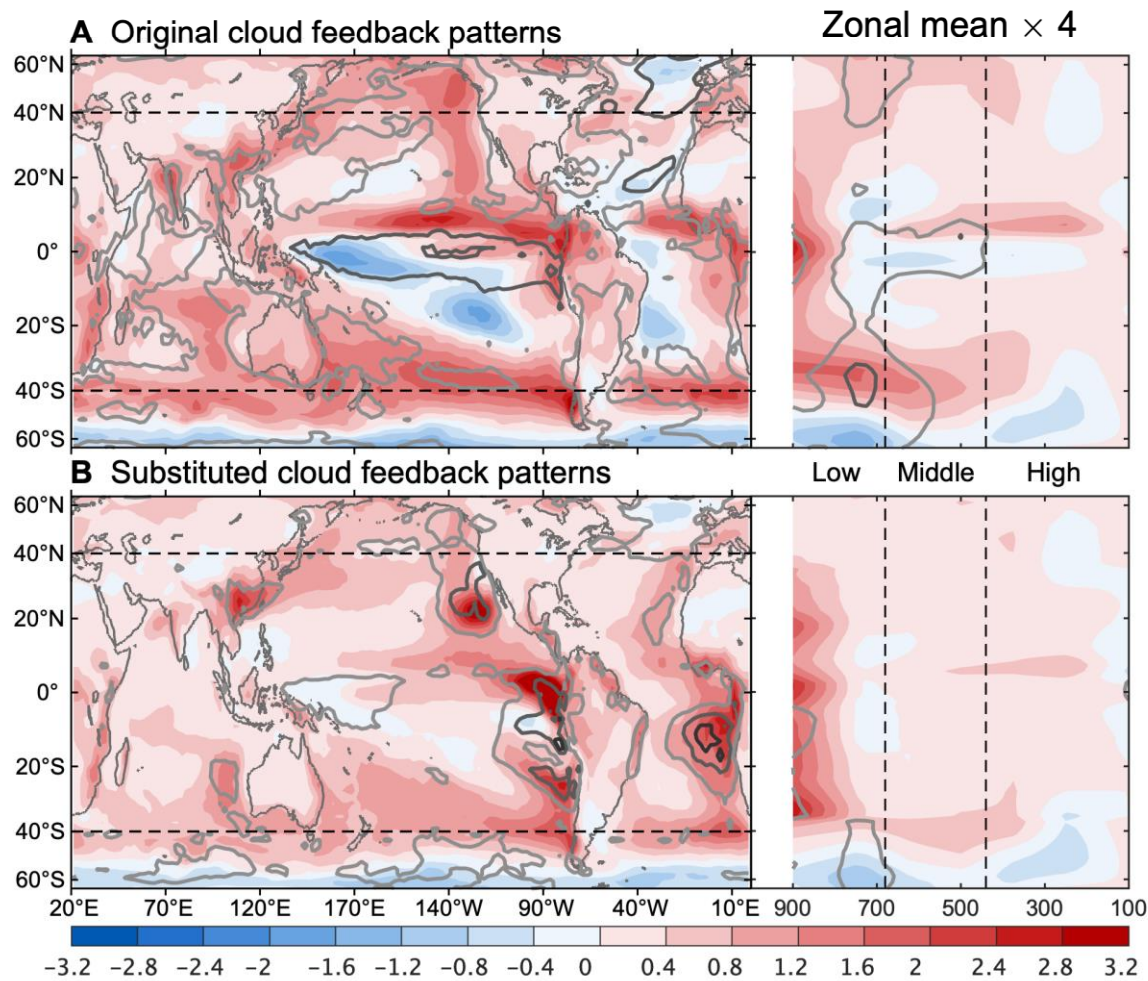
Figure 5. Comparisons of the horizontal (left) and zonal-mean (right) distributions between cloud feedbacks (W m^{-2} K^{-1}).

We compare the (*A*) original (λ) and (*B*) substituted (λ_s) feedbacks. The ensemble mean (shading) is presented with the intermodel standard deviation (contours, CI: 1 W m^{-2} K^{-1}; darker indicates a greater value). The dashed lines mark the extended tropics for 40°S–40°N and divide the cloud types by altitude at 440 and 680 hPa. Here we use the monthly-mean cloud radiative kernels, SST and cloud observations, and 21 CMIP simulations normalized by the global-mean surface (air) warming. After observational substitution by the projected sensitivity, which scales the percentage cloud sensitivity and corrects for biases in the fractional kernels, the cloud feedback patterns favor the eastern tropical basins, become more positive and the most uncertain due to stronger reductions in non-obscured low clouds, but appear much weaker and quieter elsewhere, e.g., in the warm pool and high latitudes of the North Atlantic, while the effects of middle and high clouds are almost eliminated in both the mean and spread.
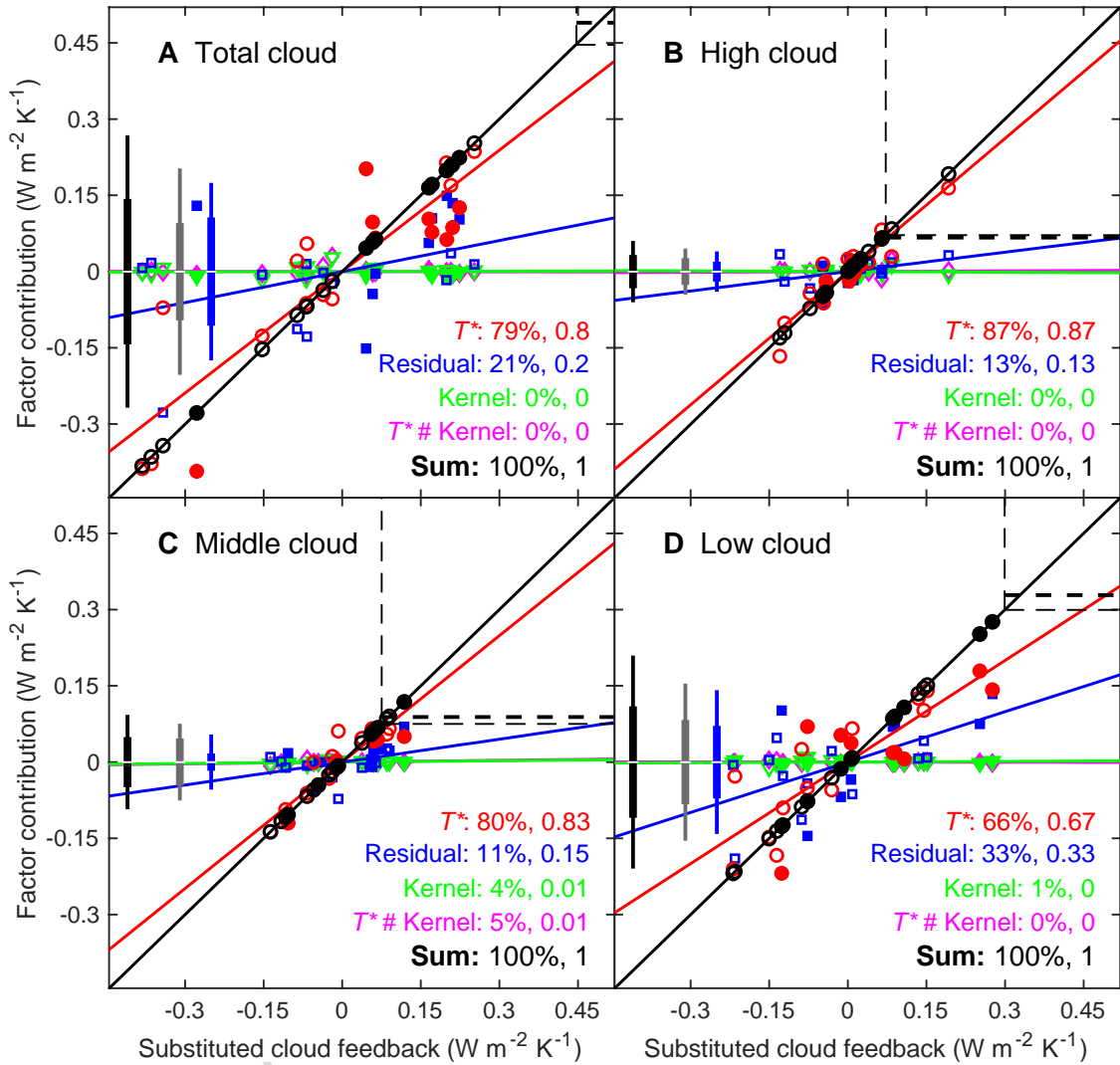
Figure 6. Intermodel scatterplots of the substituted cloud feedback λ_s (W m^{-2} K^{-1}) and its factor effects (color) evaluated using the attribution procedure, including the accumulation of the first 12 SVD modes controlled by the T^*, residual factors, fractional kernel biases, and nonlinear T^*-kernel interaction.

They are for (*A*) total, (*B*) high, (*C*) middle, and (*D*) low clouds. The symbols denote the intermodel anomalies. The filled symbols represent the nine constricted models. The black circles examine the sum of all factors and are aligned exactly along the black $y = x$ line. The dashed lines show the ensemble means: thin lines validate the balances of the substituted feedback (*x*) and the sum (*y*) of all factors, and thick lines represent the deviating eventual constraint. Error bars represent all Eq. **13** terms in turn, at the 90% (thin) and 66% (~1 standard deviation; thick) confidence levels. The cloud feedback variances (exclusive R^2 in *Methods*, %) explained by the specific factors and their sum are listed with the slopes in the corresponding regressions. Here we use the monthly-mean cloud radiative kernels, SST and cloud observations, and 21 CMIP simulations normalized by the global-mean surface (air) warming. For total and most types of cloud feedback, the SST patterns are recognized as the primary contributor and the residual factors as secondary, and the sum of all factors recovers 100% of the uncertainty.
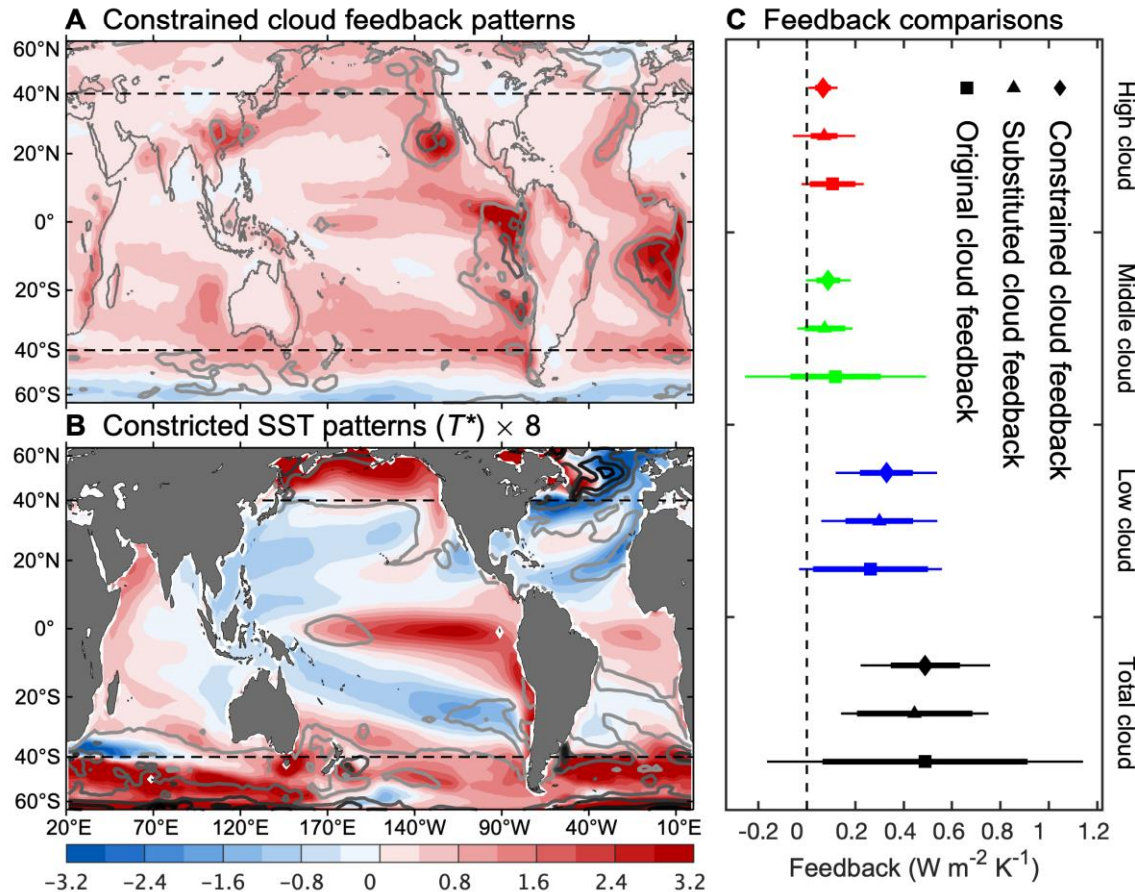
Figure 7. SST patterns and cloud feedbacks.

Horizontal distributions of (*A*) the constrained cloud feedback (W m^{-2} K^{-1}) and (*B*) the constricted SST patterns T^* (K) are shown along with (*C*) comparisons between the original cloud feedback λ (W m^{-2} K^{-1}) and that constrained in two stages. In particular, the effect of the nine model-constricted SST pattern changes shown in (*B*) is combined with that of the residual factors in (*A*). In (*A* and *B*), the ensemble mean (shading) is shown with the intermodel spread (contours, CI: 1 corresponding unit; darker indicates a greater value). The dashed lines mark the extended tropics (40°S–40°N). For each feedback in (*C*), the symbol denotes the ensemble mean, with thin and thick error bars spanning the 90% and 66% (~1 standard deviation) confidence intervals, respectively. Here we use the monthly-mean radiative kernels, SST and cloud observations, and 21 CMIP simulations normalized by the global-mean surface (air) warming. The constrained intermodel uncertainty in the global total cloud feedback reaches about two-fifths of the original.
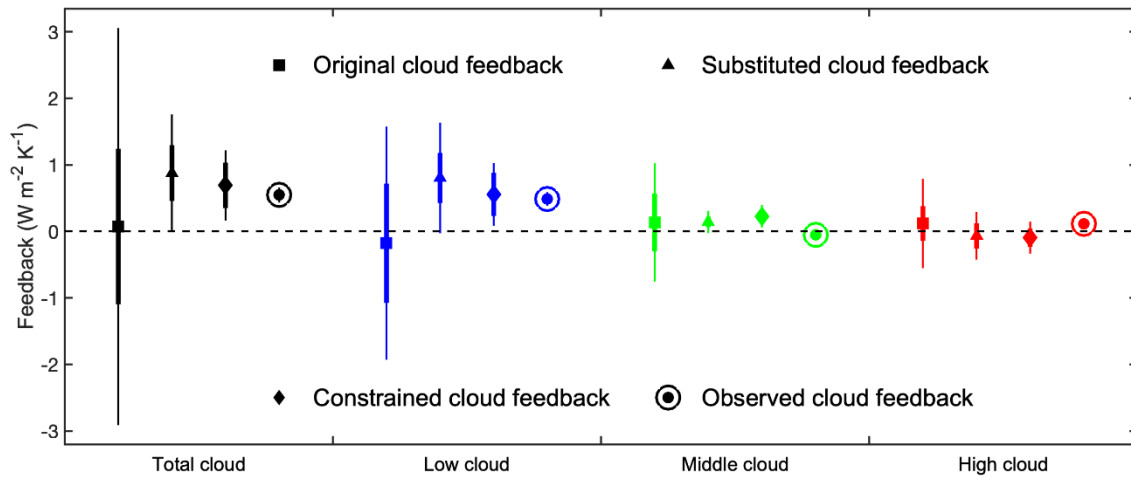
Figure 8. Same as in Fig. 7*C* but for the tropical cloud feedback computed using the 20 historical simulations during 1986–2005, and its comparison with the observed tropical feedback based on the MODIS clouds and SST suite during 2003–2022.

Apparently, the historical range of cloud feedback is extremely reduced (about three quarters) by our stagewise constraint, which covers well the observed range for the strong total and low cloud feedback, and closely overlaps with that for the weak middle and high cloud feedback.